

Control of a Multiple Source Microgrid With Built-in Islanding Detection and Current Limiting

Jeffrey M. Bloemink, *Student Member, IEEE*, and M. Reza Iravani, *Fellow, IEEE*

Abstract—An approach for the control of a voltage-sourced converter-interfaced distributed energy resource microgrid environment with multiple energy sources is analyzed and experimentally validated. The control approach is designed to operate in grid-connected and islanded modes of operation, as well as provide a smooth transition between the two modes. Additional features including islanding detection with positive feedback and dynamic overcurrent limiting are also evaluated. Validation is achieved through the results obtained from a scaled down prototype system with further results from the time-domain simulation of a medium-voltage microgrid.

Index Terms—Autonomous, control, inverter, islanding, microgrid, voltage-sourced converter (VSC).

I. INTRODUCTION

AS THE depth of penetration of distributed energy resources (DERs) increases to meet the rise in demand for electricity while reducing environmental impacts [1], microgrids will become more commonplace [2]. Sources which are part of a microgrid have unique requirements: each DER, whether a distributed generator (DG) source or a distributed storage (DS) unit, should be able to be added and removed without a significant impact on the microgrid. The microgrid should also be able to transition smoothly between grid-connected (GC) mode and islanded (IS) modes in both preplanned and emergency situations [2]–[4].

In most cases, a DER unit is interfaced to the host microgrid with a voltage-sourced converter (abbreviated as *converter* throughout this paper), creating the need for an effective method of controlling this interface converter to meet these microgrid operational requirements [5]. This paper further explores the converter control strategy introduced in [6]; a phase and magnitude variance-based controller which incorporates features necessary for operation in a microgrid environment (i.e., islanding detection, overcurrent protection, and droop control). This control strategy will be referred to throughout this paper as the voltage-controlled strategy (VCS). The intention of this paper is to further that of [6] by:

- demonstrating its use with multiple sources;

- compare and test its compatibility with sources utilizing other control methods;
- characterize the overcurrent limiting capabilities;
- discuss islanding detection tuning procedures;
- validate operation experimentally with hardware implementation.

A common approach to converter control is based on regulation of direct and quadrature (dq) current components [7] (i.e., the converter is operated as a current-controlled voltage source). This strategy will be referred to throughout this paper as the current-control strategy (CCS). It is neither necessary nor desirable that all DER units utilize the VCS in a microgrid setting, so configurations are investigated in which all units utilize the VCS; multiple VCS-based and multiple CCS-based units co-exist; or a single unit utilizes the VCS, and the remaining units utilize the CCS. The CCS approach works well when the microgrid is grid-connected, with the grid supporting the voltage and frequency at the point of common coupling (PCC) bus; however, when the microgrid is disconnected from the utility (islanded), the converter cannot maintain the voltage and frequency at the PCC [7]. In a microgrid with multiple sources, this behavior can be corrected by ensuring at least one unit utilizing the VCS (master) is present. This is commonly referred to as a master-slave control scheme and has been discussed previously in [8]–[10]. This paper explores this concept with the use of the VCS control scheme of [6]. With a VCS unit present, the frequency and voltage are supported after the transition into islanded mode by the VCS-based source while the CCS units continue to exchange real and reactive power with the microgrid. A consequence is that it is not necessary for the sources utilizing the CCS to immediately detect the islanded state. This feature is important if the CCS units are designed without the intention of coordinating with other sources in the microgrid, such as an aggregate of a large number of photovoltaic interface inverters.

Overcurrent protection is achieved by applying static or dynamic limits to the commanded output voltage magnitude. Islanding detection is achieved through forced-destabilization of the microgrid upon islanding; exploiting the fact that the sources dominantly determine the PCC bus voltage in islanded mode [11]. This destabilization affects the converter terminal voltage and can therefore be detected locally. Hardware testing is done with two inverter-interfaced sources in order to verify controller features. Further insight into the performance and behavior of the proposed VCS is achieved through the time-domain simulation of a larger scale model with five inverter-interfaced sources.

Manuscript received November 27, 2011; revised February 23, 2012; accepted April 30, 2012. Date of publication August 24, 2012; date of current version September 19, 2012. Paper no. TPWRD-01011-2001.

J. Bloemink is with the Electrical Engineering Department, Imperial College, London, SW7 2AZ, U.K. (e-mail: j.bloemink@imperial.ac.uk).

M. R. Iravani is with the Electrical Engineering Department, University of Toronto, Toronto, ON M5S 3G4 Canada (e-mail: iravani@ecf.utoronto.ca).

Color versions of one or more of the figures in this paper are available online at <http://ieeexplore.ieee.org>.

Digital Object Identifier 10.1109/TPWRD.2012.2198497

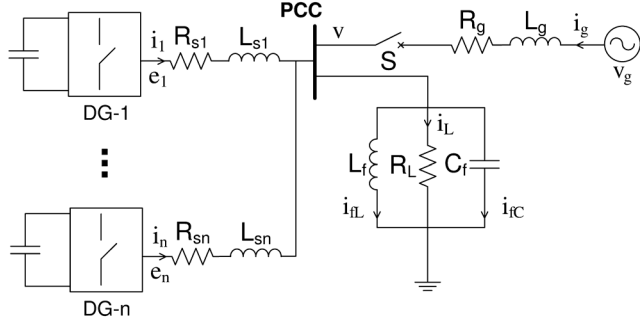


Fig. 1. Schematic circuit diagram of the test system.

II. SYSTEM DESCRIPTION

A three-phase ac microgrid with n sources (Fig. 1) is considered, with the hardware implementation containing two units ($n = 2$) and the simulated system five ($n = 5$). Each source consists of an interface converter in series with an inductor that represents the aggregate of a series filter, coupling transformer, and short line. A representative load is formed with a parallel RLC branch at the PCC.

III. CONTROLLER DESCRIPTION

Each source utilizes one of the two aforementioned control strategies: VCS or CCS. The CCS will only be briefly described here, since it is a well-established approach [5].

A. Voltage-Control Strategy (VCS)

The VCS control approach is designed to operate in grid-connected and islanded modes of operation, as well as the transition between the two. The VCS fixes voltage and frequency, operating the converter as a voltage-controlled voltage source. Once in islanded mode, the power flow is determined passively according to the load impedance.

1) *Voltage/Reactive Power Control*: A block diagram of the converter voltage/reactive power controller is given in Fig. 2. Inputs Q and $|v|$ are the measured reactive power delivered by the source and the PCC voltage magnitude, respectively. Fig. 2 reveals the integral control strategy used to achieve regulation, with controller speed dominantly determined by the gain parameter K_q . e_{mag}^i represents the change in terminal voltage to regulate to Q_{ref} , e_{mag}^p the output terminal voltage required to reach desired operation, and e_{mag} the commanded output terminal voltage magnitude after limits are applied. D_q determines droop operation. More information about how droop constants are determined for power sharing can be found in [12]. The controller is designed based on the assumption that the reactive power flow is dominantly determined by the magnitude of the voltages at the converter terminals and PCC bus. Inspection of the controller block diagram yields

$$e_{mag}^p = E_s - D_q Q + \frac{K_q}{s}(Q_{ref} - Q) + \frac{K_q}{s}G(s)|v|. \quad (1)$$

When in islanded mode, it is necessary to disable reactive power control and allow the flow of reactive power to be determined by the load. This is done by setting $K_q = 0$ upon islanding detection and confirmation [6]. E_s , the voltage setpoint,

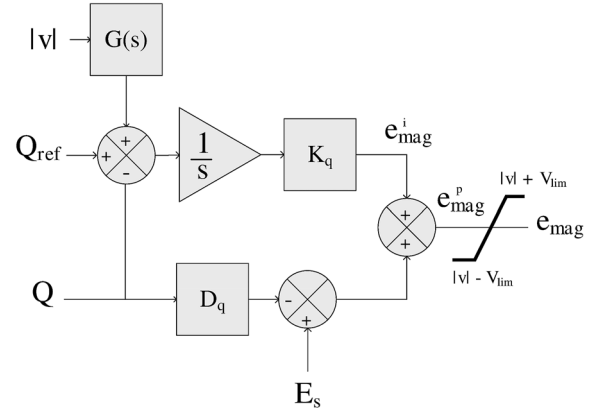


Fig. 2. VCS reactive power/voltage-controller block diagram.

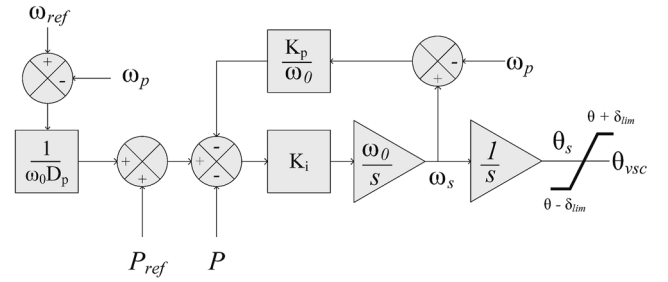


Fig. 3. VCS real power/frequency-controller block diagram.

is determined depending on network parameters to allow the system to operate within the allowable limits once the system has islanded and the reactive power controller has been disabled. Further information regarding integral control of reactive power in microgrids can be found in [13] and [14].

Voltage Droop Control: The droop term of (1), $D_q Q$ is used to minimize interaction among sources in a multiple source configuration and enable reactive power sharing [12]. It ensures that the control scheme meets performance requirements regardless of the number of sources present [2].

2) *Frequency/Real Power Control*: A block diagram of the frequency/real power controller is given in Fig. 3. ω_p , ω_s , and ω_0 are the PCC bus, converter terminal, and system nominal frequencies, respectively. The gain term K_p is used to control power regulation speed. D_p represents the real power droop constant. The term K_i can also affect the controller regulation speed but is generally used to refine second-order transient behavior of the controller. Finally, the controller outputs a frequency ω_s that is integrated to θ_s , and limited appropriately to form the converter terminal voltage phase angle θ_{vsc} .

Proper operation of this controller is dependent on three factors:

- the real power flow and frequency are dominantly determined by the relative phase of the converter terminal voltage e ;
- when in grid-connected mode, the utility dominantly determines the system frequency ω_p ;
- when in islanded mode, the source must determine the system frequency ω_p .

TABLE I
OPERATIONAL LIMITS FOR GRID INTERACTION (UL1741)

PCC Voltage (pu)	PCC Freq (Hz)	Time to Disconnect
$V \leq 0.50$	rated	0.16s
$0.50 \leq V < 0.88$	rated	2s
$0.88 \leq V \leq 1.10$	$59.3 \leq f \leq 60.5$	N/A
$1.10 < V < 1.20$	rated	1s
$1.20 \leq V$	rated	0.16s
rated	$f < 59.3$	0.16s
rated	$f > 60.5$	0.16s

This controller can be expressed symbolically as

$$\frac{1}{\omega_0 K_i} \frac{d\omega_s}{dt} = P_{ref} - P + \frac{1}{\omega_0 D_p} (\omega_{ref} - \omega_p) + \frac{K_p}{\omega_0} (\omega_p - \omega_s). \quad (2)$$

While in grid-connected mode, the assumption $\omega_p = \omega_{ref}$ is used and (2) is reduced to

$$\frac{1}{\omega_0 K_i} \frac{d\omega_s}{dt} = P_{ref} - P + \frac{K_p}{\omega_0} (\omega_p - \omega_s). \quad (3)$$

Since the power flow will not be constant if the frequency of the source ω_s and PCC bus ω_p differ, the equilibrium condition for the grid-connected mode must be $\omega_s = \omega_p$ and $P = P_{ref}$. Re-emphasizing the initial assumption that the source does not have a significant effect on the PCC frequency, it can be concluded that the source frequency ω_s will settle to the reference frequency.

When in islanded mode, the assumption $\omega_p = \omega_s$ yields

$$\frac{1}{\omega_0 K_i} \frac{d\omega_s}{dt} = P_{ref} - P + \frac{1}{\omega_0 D_p} (\omega_{ref} - \omega_s). \quad (4)$$

In this mode, the settling point of the real power/frequency controller depends primarily on the load for a relatively constant PCC voltage. The system will settle to a frequency so that the difference in the real power demand of the load and the reference power control signal is offset by a small, but acceptable, frequency droop. The power-frequency droop characteristic can be set by adjusting D_p . The droop characteristic also determines the load sharing profile in a multiple source configuration [2].

3) *Islanding Detection*: The control system determines whether the system has islanded based on the value of the PCC voltage $|v|$. For example, if $|v|$ drops below 0.5 p.u. for more than 0.16 s, the source assumes the system has or will soon island from the grid. In a preplanned islanding scenario, however, the real and reactive power exchanged with the grid is usually brought to zero prior to islanding to reduce transients and so the system will likely not violate the performance boundaries of Table I [15]; the source will therefore have no indication that the microgrid is in islanded mode, making an islanding detection method necessary.

By adding a positive feedback branch to the reactive power and voltage controller of Fig. 2, it is possible to introduce a destabilizing effect once the PCC breaker has opened; exploiting the fact that the sources dominantly determine the PCC bus voltage in islanded mode, while the utility does so in grid-connected mode. This islanding detection method is similar to the Sandia voltage shift (SVS) [11] method, with the difference being that the positive feedback is applied to reduce

the voltage level at the converter output to induce a drop on $|v|$ rather than the SVS strategy of reducing current reference levels to lower $|v|$.

The function $G(s)$ is given as

$$G(s) = \frac{K_d s}{(1 + T_1 s)(1 + T_2 s)}. \quad (5)$$

The bandpass filter response of (5) limits the spectral range for which disturbances can destabilize the system. The parameters of (5) must be adjusted so that the positive feedback system does not amplify the harmonics associated with the PCC voltage under normal operating conditions in grid-connected mode, but also responds quickly enough to satisfy islanding detection speed requirements. The selection of the parameters in (5) is more forgiving with increasing stiffness of the grid connection, allowing the detection speed to be increased without any undesirable effects in grid-connected mode. An example of parameter selection is given later in Section VI-D.

With this islanding detection system in place on the VCS units, CCS-based sources need not be aware of the microgrid status to maintain a stable system frequency and voltage. After the islanding has taken place, low bandwidth communication links can be used to set a power reference for dispatchable sources. It is also possible to add droop control functionality to the CCS units to facilitate power sharing. This was not considered in this paper as CCS units are considered to be uncoordinated, or “dumb” sources.

4) *Overcurrent Limiting*: It is acknowledged that most voltage-sourced converters will have an independent current-limiting system in place in order to prevent device damage, which will typically be in the range of 1–2 p.u. at steady state; however, the peak transient current allowed by this fail-safe system will depend on the device and filter topology [16]. This current limiting scheme under discussion is intended to limit peak transient currents from the perspective of the control system, allowing for controlled current limiting with all device types.

The commanded output voltage magnitude e_{mag} can be limited to a band around the PCC voltage magnitude $|v|$ according to (6). By limiting the voltage difference from the PCC, peak fault currents can be limited at the cost of a reduction in the control range of the reactive power regulator

$$e_{mag} = \begin{cases} |v| - V_{lim}, & \text{for } e_{mag}^p \leq |v| - V_{lim} \\ E_s - D_q Q + \frac{K_q}{s} (Q_{ref} - Q), & \text{for } |v| - V_{lim} < e_{mag}^p < |v| + V_{lim} \\ |v| + V_{lim}, & \text{for } e_{mag}^p \geq |v| + V_{lim}. \end{cases} \quad (6)$$

In addition, by limiting θ_{VSC} to within a band around the PCC voltage phase according to (7), peak fault currents can also be reduced

$$\theta_{VSC} = \begin{cases} \theta_{pcc} - \delta_{lim}, & \text{for } \theta_s \leq \theta_{pcc} - \delta_{lim} \\ \frac{1}{s} \omega_s, & \text{for } \theta_{pcc} - \delta_{lim} < \theta_s < \theta_{pcc} + \delta_{lim} \\ \theta_{pcc} + \delta_{lim}, & \text{for } \theta_s \geq \theta_{pcc} + \delta_{lim}. \end{cases} \quad (7)$$

By making these limits dynamic instead of static, peak fault currents can be lowered further. Dynamic limiting is achieved by making the limits δ_{lim} and V_{lim} inverse-square proportional to the converter output current magnitude, $|i_n|$, according to (8).

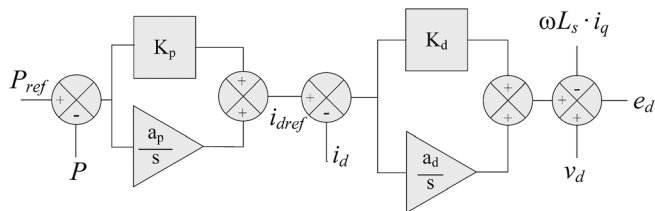


Fig. 7. CCS reactive power/voltage-controller block diagram.

TABLE II
ASSIGNED POWER RATINGS FOR INDIVIDUAL UNITS
OF EXPERIMENTAL MICROGRID

Source	P_{rated} (pu)	Q_{rated} (pu)
1	0.3	0.15
2	0.7	0.3

The criteria are summarized in Table I. The smaller deviations from the nominal operation conditions will be referred to throughout the remainder of the paper as “soft-violations,” and the extreme deviations will be referred to as “hard-violations.”

V. HARDWARE IMPLEMENTATION AND RESULTS

As a proof of concept, an experimental setup containing two sources connected in parallel to a single aggregate load was constructed. The parameters for the experimental system are given in Table V of the Appendix.

The passive elements of the circuit were constructed as follows: the line filters, PCC-utility impedance, and the inductive portion of the load were realized with single-phase inductors. The capacitive branch was implemented with a set of three Y-connected adjustable ceramic capacitors per source. The real portion of the load was realized with a step-adjustable load bank, allowing for abrupt load switching. Two-level insulated-gate bipolar transistor (IGBT)-based voltage-sourced converters were used to represent the sources. The control system and PWM were realized with an RTLinux-based controller, allowing the control systems under study to be developed in C [18]–[20].

In the laboratory-built prototype, the microgrid contains two converter-interfaced sources connected in three-phase configuration. While both units are physically rated to deliver the same amount of power, the nominal operating point of Source 2 will be considered to be lower than Source 1 in order to emulate the presence of a varied set of distributed generators. These assigned ratings are shown in Table II. Also to this end, all of the tests discussed in this section utilized different interface filter ($L_{s1} = 5$ mH, $L_{s2} = 10$ mH). Parameters for the three-phase experimental microgrid are shown in Table V.

The following different control combinations were explored with the experimental prototype system:

- VCS-VCS: Sources 1 and 2 controlled with the VCS;
- VCS-CCS: Sources 1 controlled with the VCS, and source 2 controlled with the CCS.

Both controller combinations exhibited similar behaviour for most tests performed; thus, unless stated, the results shown and described are for that of the VCS-VCS combination. Differences

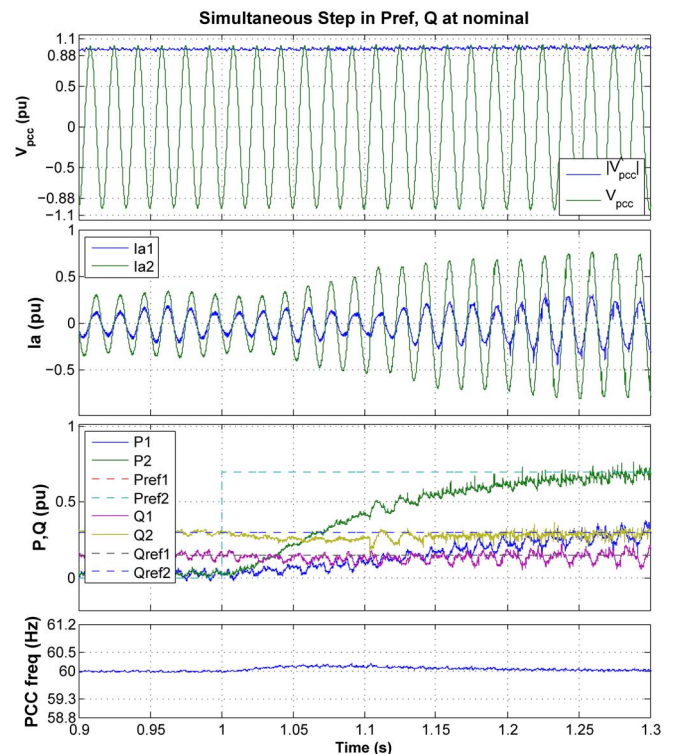


Fig. 8. Real power step response.

in behavior between the VCS and CCS controlled sources will be highlighted.

A. Grid-Connected Mode

1) *Controller Step Response*: Both the real and reactive power controllers were tuned to achieve a damped step response with a time constant of approximately 100 ms. The controller parameters used are given in Table V. Initial control gains were obtained using an ideal small-signal model of the experimental system as in [21].

The resulting waveforms for a simultaneous step in both values of P_{ref} to nominal at $t \approx 1$ s are shown in Fig. 8. Coupling between the real and reactive power controllers is made apparent in this test case as the reactive power deviates from its nominal point during the power-controller transient time. Both sources are brought out of synchronism with the PCC briefly while θ_{VSC} settles. This has a slight effect on the measured PCC frequency but is still maintained within the bounds defined in Section IV. The PCC voltage was observed to deviate slightly due to the low X/R ratio of the filter and feeder line.

Fig. 9 shows the resulting waveforms for a simultaneous step in both values of Q_{ref} to nominal at $t \approx 1$ s, with the real power references kept constant at their nominal values. Note the coupling between real and reactive power flow (i.e., there is a disturbance in the real power flow from both sources).

It can be seen in Figs. 8 and 9 that the real power flow deviates slightly from the reference signal even when settled. This is due to the fact that the utility frequency ω_p does not match that of the reference ω_{ref} and so the initial assumption that $\omega_p = \omega_{ref}$

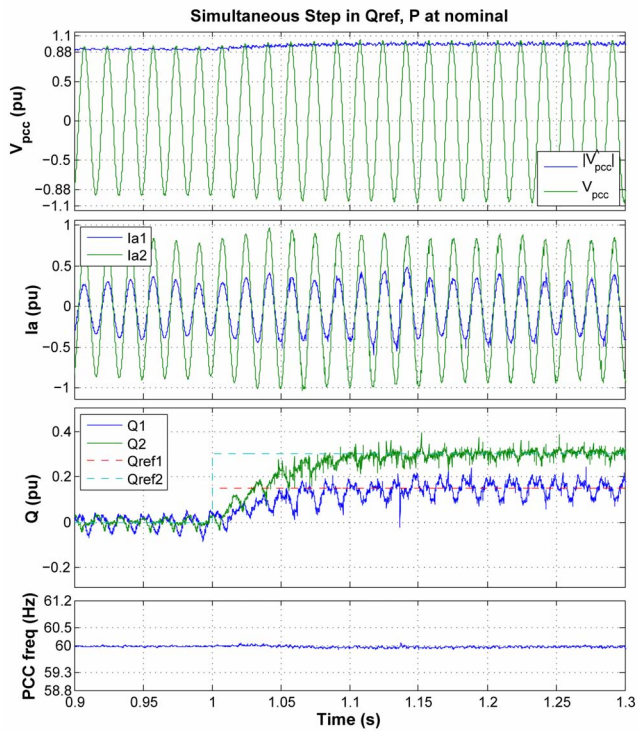


Fig. 9. Reactive power step response.

no longer holds. From (2), one can deduce that the effective reference that the real power flow will be regulated to is

$$P'_{ref} = P_{ref} + \frac{1}{\omega_0 D_p} (\omega_{ref} - \omega_p). \quad (10)$$

Since D_p has to be small for proper operation, even a slight unexpected deviation in the utility frequency can bring about a noticeable change in real power flow. This can be corrected simply by adjusting ω_{ref} to meet that of the utility. Adjusting ω_{ref} will also affect the overall system frequency in islanded mode. In the case of the sources utilizing the CCS, this problem is, of course, not observed as the real power flow is not dependent on ω_p .

2) *Load Switching*: The load switching cases considered are the complete removal of the real portion of the load (full load to no load) or the addition of the rated real power load from a no load condition (no load to full load).

The resulting waveforms for no load to full load at $t \approx 1.45$ s are shown in Fig. 10. To outline the difference in behavior between the VCS and CCS for a load switching event, the mixed combination is used to control the sources (i.e., VCS-CCS). Contrary to the VCS-controlled sources, the CCS-based units are not noticeably affected by the load switching event.

Prior to the load being introduced to the system, the source is exporting rated power to the utility. In the source utilizing the VCS, the real power flow and output current increase significantly with the addition of the load (from approximately $t = 1.45$ s), but settles to the nominal value within approximately 150 ms. The CCS-based system is able to maintain the power flow throughout the event. The reason why the CCS output current and power do not falter with the load change event is because the fast dq-current inner control loop is tuned

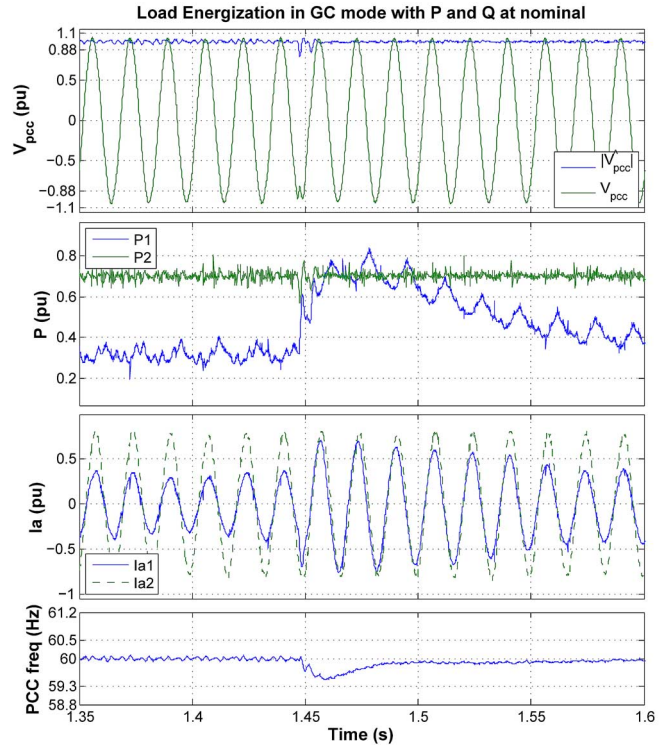


Fig. 10. Load energization in grid-connected mode.

to respond much more quickly relative to the slower real power control loop.

In the case of the VCS, the connection of the real portion of the load changes the flow of current from the grid instantaneously to the resistive load. This implies an instantaneous change in θ , and the phase difference between θ and θ_{VSC} is also instantaneously increased; hence, power flow changes until the phase difference can be readjusted to meet that of the real power setpoint. The VCS does not have a fast internal current control loop to limit the current and therefore requires a comparatively longer time to recover. If necessary, this current excursion can be limited further by adjusting the limits on θ_{VSC} to provide a similar effect to that demonstrated in Section VI-C.

B. Transition to Islanded Mode

Transition from grid-connected to islanded-mode operation was performed under two pre-islanded conditions: one in which the sources are supplying full apparent power to the load, and one in which the source is supplying zero apparent power to the load. The experimental system was able to successfully transition in both cases. The latter case, which will be referred to as the unplanned islanding scenario, is a more extreme case due to the fact that both sources are required to transition from supplying no apparent power to rated apparent power upon islanding (opening of the PCC breaker) in order to meet the load demand.

The resulting waveforms for the unplanned islanding scenario for the VCS-VCS combination are shown in Fig. 11. In these tests, the microgrid is disconnected from the utility at the PCC at $t \approx 1.0$ s. The droop constants for the VCS-based systems D_p have been calibrated such that the frequency does not

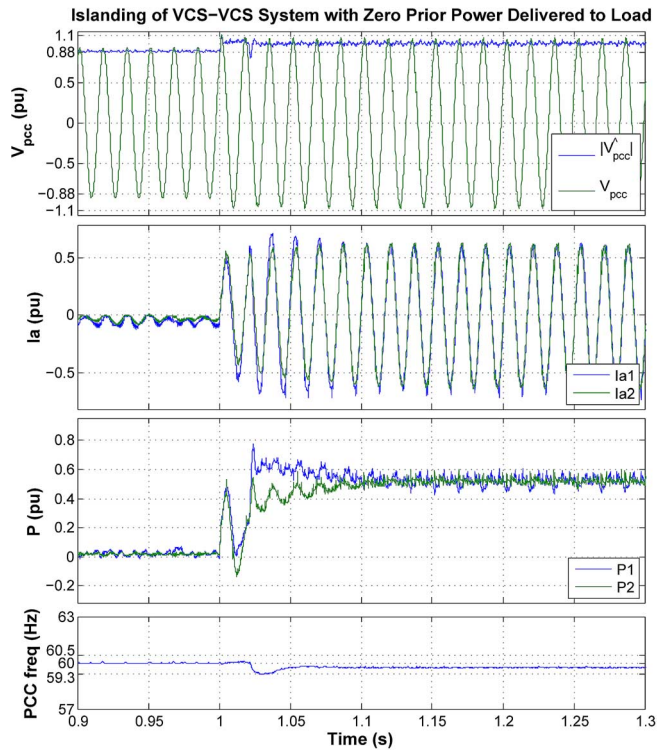


Fig. 11. VCS-VCS: transition from grid-connected to islanded mode.

deviate past that specified in Table I and that the load sharing profile suits the assigned ratings of each source in Table II. The voltage setpoint E_s ensures the nominal operating point is reached upon islanding.

Fig. 12 examines the real power flow and frequency dynamics during the unplanned islanding event. The frequencies shown are those of the individual sources, and the value to which they settle becomes the microgrid PCC frequency ω_p . The case in which the droop constants have been adjusted to different values so that the power flow is different has slightly higher frequency excursions due to the larger step in real power delivered by Source 2 and is shown in the lower portion of Fig. 12. This comparison serves to demonstrate that the droop constant can be adjusted to ensure that sources will deliver their rated amount of power in islanded mode.

Fig. 13 shows the resulting waveforms for the same test done with the VCS-CCS controller combination. The major observed difference of the VCS-CCS system is when the system enters islanded mode, the CCS-based source will deliver zero apparent power. It is therefore necessary to adjust the reference to meet the real power demand. This postislanding adjustment is performed at $t \approx 1.5$ s in Fig. 13. This implies that the VCS-based system must fully support the load until the CCS-based source realizes the system has islanded. Once the adjustment to reference power is made and controllers have settled, both perform similar to the previous test.

C. Islanded-Mode Operation

1) *Load Switching*: The resulting waveforms for the case of (full load to no load) are shown in Fig. 14.

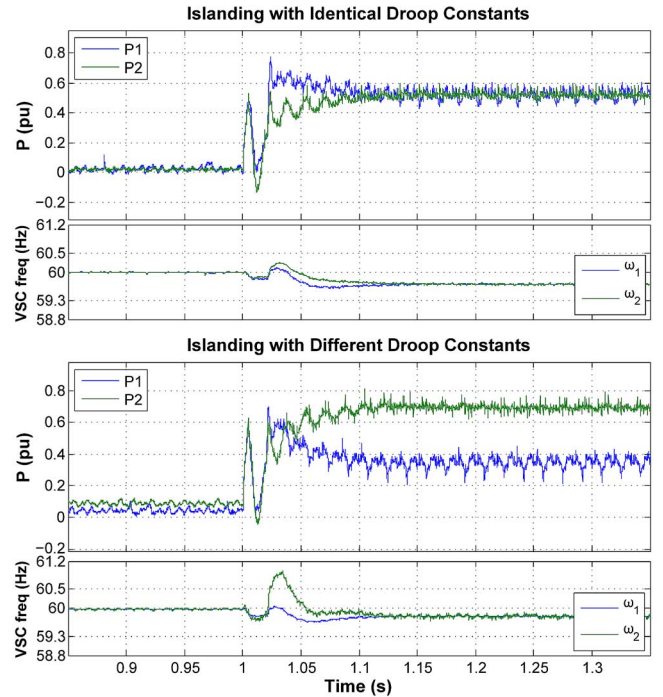


Fig. 12. VCS-VCS: Effect of droop constant on islanding transition behavior and settling point.

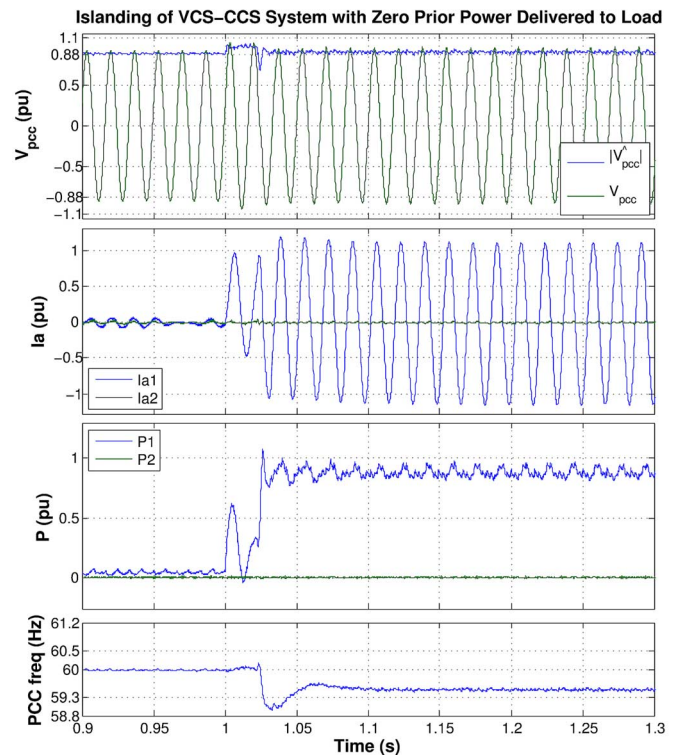


Fig. 13. VCS-CCS: Transition from grid connected to islanded mode.

In the VCS-VCS combination, the real power flow drops to almost zero immediately. The nonzero real power delivered is due to the losses associated with the reactive portion of the load. The system also recovers quickly for the case in which the real portion of the load is reintroduced instantaneously (full load to

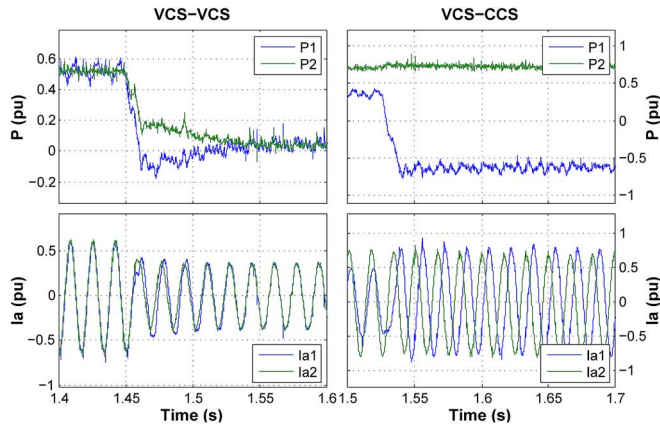


Fig. 14. Load dropping in islanded mode for the VCS-VCS and VCS-CCS combination.

no load). To maintain the PCC voltage at its nominal value, E_s can be adjusted as needed. Smaller changes in loading resulted in less pronounced transients.

The VCS-CCS system behaves differently upon disconnection of the load at $t \approx 1.5$ s: since the CCS-based source is regulating P_n to 0.7 p.u., disconnecting the load entirely causes P_n from the CCS unit to be rectified through the VCS-based source, accounting for the negative real power flow seen in the bottom of Fig. 14. In a real-world scenario, sources will likely only allow unidirectional power flow causing the CCS-based source to fail to meet P_{ref} .

VI. SIMULATION RESULTS

Additional test cases were analyzed based on time-domain simulations using the PSCAD/EMTDC software package to demonstrate the behavior of the controller in extreme fault scenarios that could not be realized in the laboratory, and to further test the overcurrent limiting and islanding detection features of the VCS.

The parameters of the simulated system were scaled to represent that of a medium-voltage microgrid (13.8 kV). The controller and network parameters are given in Table III. The power ratings of the sources, on the overall system base, are given in Table III.

The following controller combinations were examined for simulation:

- *5VCS-0CCS*—all sources utilizing the VCS;
- *3VCS-2CCS*—a mix of VCS-based and CCS-based units to demonstrate compatibility/interoperability between the two control strategies;
- *1VCS-4CCS*—a master-slave scenario, with the VCS-based unit supporting the system voltage and frequency when in islanded mode, while the CCS-based units continue to operate in all network states.

Unless otherwise specified, the simulation results shown and analyzed will be for the first combination (*5VCS-0CCS*). Noteworthy differences in operation for other controller combinations will be highlighted.

TABLE III
DEFINED POWER RATINGS FOR INDIVIDUAL UNITS OF THE SIMULATED SYSTEM

Source	P_{rated} (pu)	Q_{rated} (pu)
1	0.05	0.017
2	0.25	0.085
3	0.1	0.034
4	0.45	0.154
5	0.15	0.051

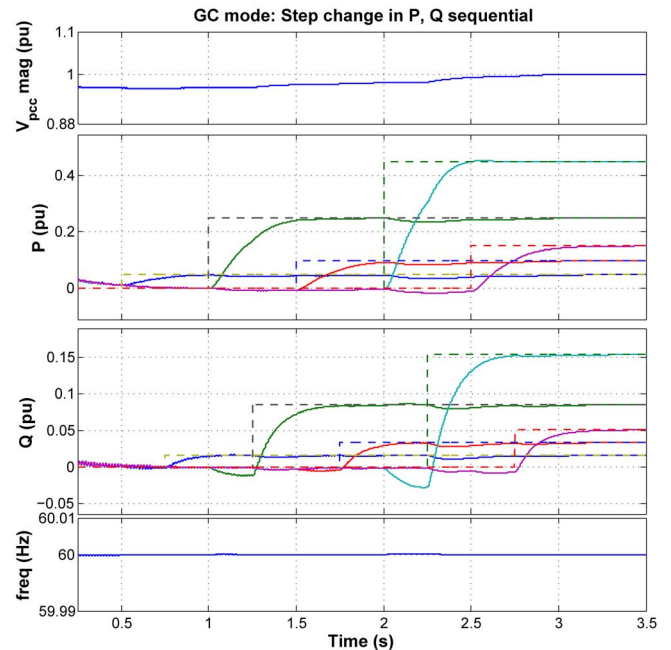


Fig. 15. Sequential step in real and reactive power to the nominal operating point for each source.

A. Controller Step Response

Fig. 15 shows the behavior of the *5VCS-0CCS* combination to a sequential step in P_{ref} and Q_{ref} for each source until the nominal operating point has been reached. Results were similar for all controller combinations (i.e., *5VCS-0CCS*, *3VCS-2CCS*, and *1VCS-4CCS*).

Coupling between the real and reactive power controllers in each source, as well as coupling between the outputs of separate sources is observed here. Despite the effects of coupling, v and w_p do not deviate from the acceptable region of operation. Fig. 15 shows the resulting waveforms.

B. Fault Transitions

The ability of each source to detect the presence of a fault, transition to islanded-mode, and reach the nominal operating condition such that the local load does not experience any interruptions is examined in this section.

Fig. 16 shows the resulting waveforms for the case in which the microgrid is islanded due to an L-L-L-GND fault outside the microgrid (i.e., the fault is isolated when the PCC is disconnected from the grid). The fault is introduced at $t = 0.5$ s, and the microgrid is islanded 0.16 s, following the detection of a voltage drop below 0.5 p.u., in accordance with Table I. The instantaneous PCC voltage and filtered magnitude ($\tau = 0.01$ s) are shown. Upon islanding, the PCC voltage level is restored to its nominal value, and real and reactive power flow reach their

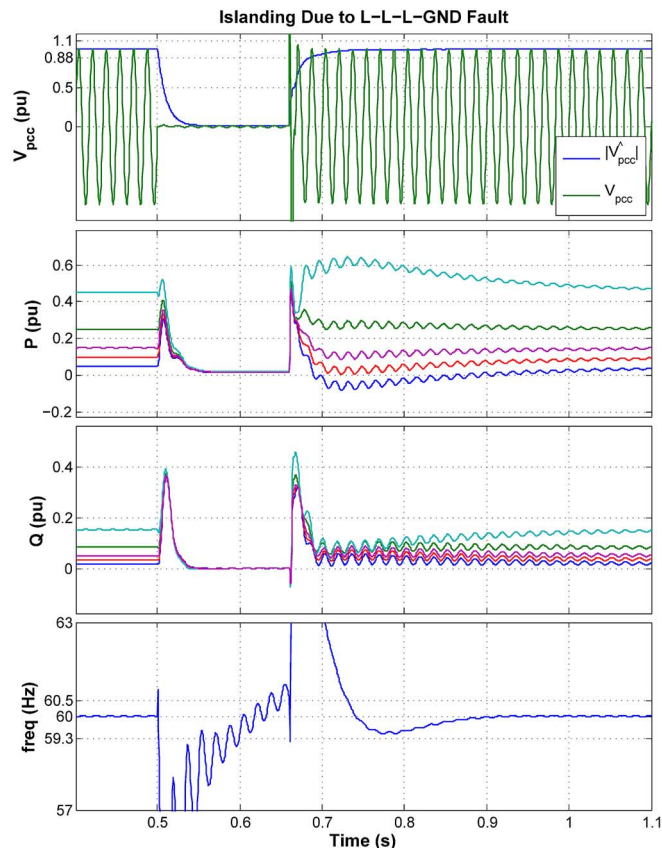


Fig. 16. Islanding of the system due to the three-phase fault for simulation with and without instantaneous islanding detection.

steady-state values within approximately 350 ms. The system was also observed to recover through islanding when exposed to other fault types, such as: L-GND, L-L-GND, L-L, and L-L-L.

C. Overcurrent Limiting

Applying dynamic limits was observed to significantly reduce the peak source line currents I_{max} , during the fault. The resulting source output currents during an L-L-L fault in grid-connected mode are given in Table IV for the cases of no limits set and dynamic overcurrent limits enabled. The static limits are set as $\delta_{lim} = 20^\circ$, $V_{lim} = 0.1$ p.u. and $T_d \approx 0.05/60$, while the dynamic relationship of (8) tightens the limits further.

These results are consistent with the maximum bounds on peak fault current limits discussed in Section III-A-IV. It is noted that the worse-case fault event instant cannot be achieved for all parallel-connected sources, especially those with different parameters. This is reflected by the varying peak fault current levels observed from this simulation. Also noted is that the current rating contribution I_{rated} in (9) corresponds to Table III and not 1.0 p.u. on the system base, thus further reducing the maximum peak fault current.

A plot of the total fault current contribution from all sources during an L-L-L-GND fault event, with overcurrent limiting, both enabled and disabled, is shown in Fig. 17. With dynamic limiting disabled, the combinations with CCS-based units present (i.e., 1VCS-4CCS and 3VCS-2CCS) have lower fault currents. Enabling the proposed dynamic overcurrent

TABLE IV
COMPARISON OF MAXIMUM FAULT CURRENTS WITH AND WITHOUT THE DYNAMIC CURRENT LIMITER ENABLED FOR A L-L-L-GND FAULT

	I_{max} (pu)					
	5VCS-0CCS		3VCS-2CCS		1VCS-4CCS	
Source	Off	On	Off	On	Off	On
Unit 1	2.41	0.28	2.39	0.27	2.40	0.28
Unit 2	2.53	0.82	2.52	0.29	0.49	0.49
Unit 3	2.44	0.45	0.19	0.19	0.19	0.19
Unit 4	2.67	1.28	0.53	0.53	0.88	0.53
Unit 5	2.47	0.59	2.45	0.57	0.29	0.29
Total	12.51	3.35	7.81	1.63	3.32	1.61

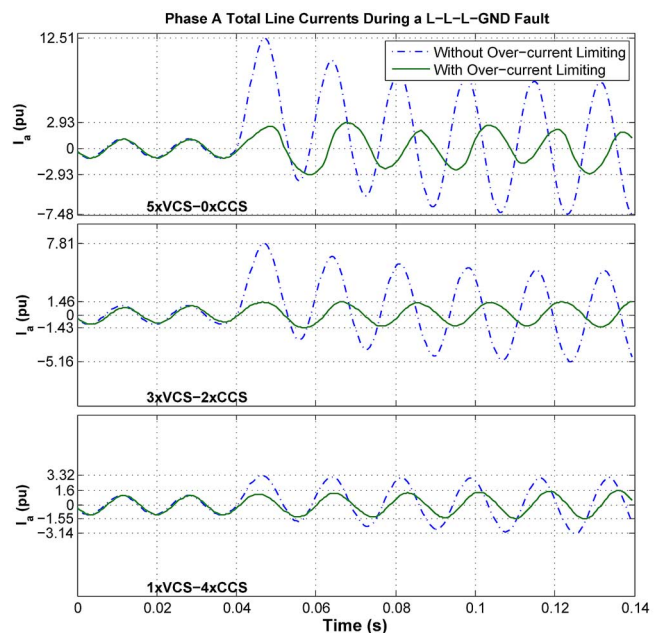


Fig. 17. Comparison of total fault current in phase A with and without dynamic limiting during the L-L-L-gnd fault event for all three system configurations.

limiting scheme shows comparable results for all controller combinations.

D. Islanding Detection Tuning and Results

For all system configurations, the parameters T_1 and T_2 are selected for a frequency band response of 1–10 Hz, which ensures that dc steady-state error signals (dq components) and negative-sequence oscillations are rejected by the positive feedback path, but other low-frequency excursions are not. The upper limit ensures that any negative-sequence components and switching harmonics are also not amplified via the positive feedback path. The gain K_d should be set for each source to achieve an acceptable islanding detection time. The criteria limiting the increase of detection speed is the stability of the system in grid-connected mode. Suitable selection of K_d will depend on the load and the grid short-circuit ratio (SCR), which is a metric for grid coupling strength and, as such, the procedure specified in this section should be adapted to the system parameters of the reader.

Fig. 18 shows the closed-loop PCC voltage disturbance gain at the frequency with peak magnitude f_d in the positive feedback transfer function $G(s)$. Included in this figure are disturbance gains from time-domain simulations of the control system

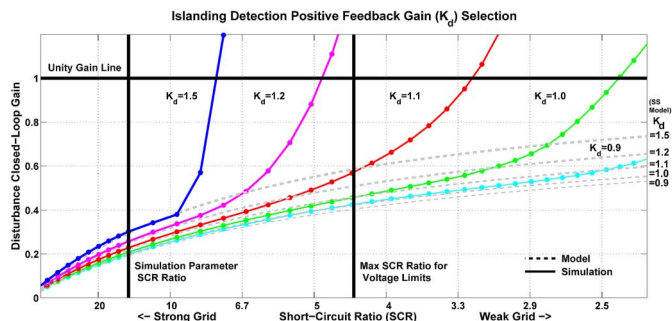


Fig. 18. Simulation system stability for different positive feedback gains as a guideline for positive feedback tuning (single VCS system).

and plant using a disturbance with a magnitude of 1 at frequency f_d . Also included are linearized small-signal models for multiple values of K_d , shown to emphasize the limitations of approximating positive feedback dynamics, as above a certain point model states require a large-signal model to accurately represent the system due to the lower disturbance rejection associated with a higher K_d or weaker grid coupling (lower SCR). A large source of inaccuracy is the small signal representation of voltage magnitude, which is highly dependent on the large signal operating point. Also shown in Fig. 18 is the SCR of the simulation system and the maximum SCR for which the PCC voltage is supported within the limits specified in Table I. The latter is included to indicate the minimum reasonable SCR for which the positive feedback system should be designed for, which allows for network reconfiguration without the sources driving the system to instability, making the overall control more robust.

Above the unity-gain line, disturbances will be reinforced by the positive feedback path and, therefore, drive the system to instability. The goal is to select a K_d so that the system is stable in grid-connected mode (high SCR) and unstable in islanded mode (open circuit, or zero SCR), allowing the aforementioned margins for network reconfiguration. For the values presented in Fig. 18, it is seen that $K_d = 1.0$ is a suitable choice to start. From there, K_d can be further increased to reduce islanding detection time.

The values specified apply to systems with a single VCS-based unit. The CCS-based units do not possess any positive feedback-based islanding detection and, as such, there are fewer units to force the voltage outside the performance limits (a phenomena described in Section III). Thus, for a given value of K_d , the 1VCS-4CCS system will be more stable, but slower and the 5VCS-0CCS system will be closer to the instability region, but perform islanding detection more quickly. This is demonstrated in Fig. 19. The 3VCS-2CCS system, with the same K_d values used for each VCS unit, takes approximately 0.49 s while the 5VCS-0CCS system does so in 0.39 s. In these results, the 1VCS-4CCS system is altered with a higher value of K_d so that its islanding detection time is comparable to that of other system configurations.

These simulations demonstrate a scenario in which the sources are not exchanging any real or reactive power with the utility grid, which represents the most difficult scenario for islanding detection after the PCC breaker is opened.

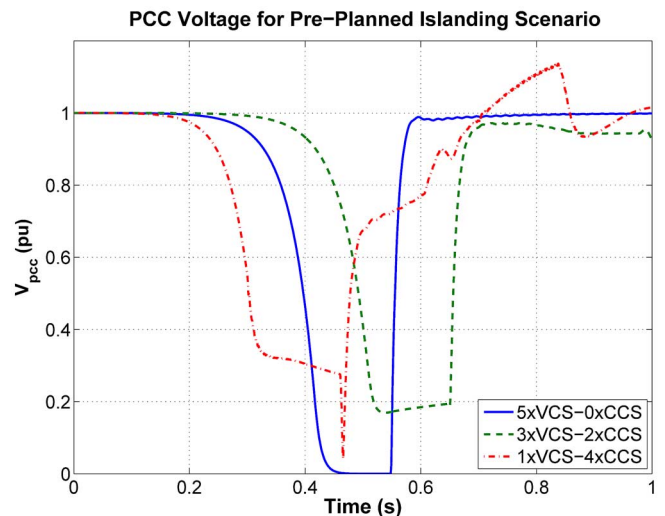


Fig. 19. Simulation results showing positive feedback islanding detection for all system configurations considered.

An issue associated with the presence of CCS-based sources after islanding is that they are still attempting to deliver their reference power while the system is islanded. A solution to this problem is to disable the CCS-based units once the PCC voltage is forced below 0.5 p.u. In the waveform for the 1VCS-4CCS system of Fig. 19, this has been done in order to demonstrate proper operation of the system. Prior to islanding, the sole VCS-based system was configured to deliver the majority of the real and reactive power (0.45 p.u.), so that the CCS-based sources do not support the PCC voltage by delivering significant real and reactive power, thereby preventing or delaying islanding detection. This is a disadvantage for systems containing a single VCS-based source with islanding detection.

It is also observed that the systems containing CCS-based units do not recover immediately once the islanded status is confirmed. Thus, it is concluded that the presence of CCS-based units is not ideal when this method of islanding detection is used. It is possible, however, that the CCS-based units be designed to reinforce the voltage drop as well using the SVS method [11]. Using the same approach as in the VCS units would allow all units to contribute to islanding detection.

Depending on the microgrid load performance requirements, another advantage to the positive feedback detection method is a possible decrease in the time before islanding due to a fault. For minor voltage sags or single-phase faults that would normally present an unacceptable soft violation to sensitive loads, for which the PCC breaker will isolate within 1 or 2 s, the positive feedback loop will reinforce these disturbances by raising or lowering the converter terminal voltage. The positive feedback branch effectively turns the soft violation into a hard violation and reduces the time taken to reach the nominal operating conditions by transitioning the entire microgrid into islanded mode more quickly overall.

VII. CONCLUSION

A simplified and scaled down prototype system was shown to operate as expected for various tests. Further simulations indi-

TABLE V
MEASURED AND DEFINED SYSTEM/CONTROLLER PARAMETERS

Parameter	Description	Experimental	Simulation
V_{base}	Base voltage ($V_{l-l,RMS}$)	115	13800
S_{base}	Base power (kVA)	1.15	2000
I_{base}	Base current (A_{RMS})	6.64	83.67
Z_{base}	Base impedance (Ω)	8.7	95.22
ω_{base}	Base frequency ($\frac{rad}{s}$)	$2\pi \cdot 60$	$2\pi \cdot 60$
K_p	P/f Controller gain	5.0	107.6
K_i	P/f Controller gain	2.0	0.50
D_p	P/f Controller droop const	0.01	0.01
K_q	Q/V Controller gain	30	3.64
D_q	Q/V Controller droop const	0.01	0.01
E_s	Q/V Controller set point	1.27	1.165
V_{gab}	Utility voltage ($V_{l-l,RMS}$)	115	13800
R_s	Filter losses (Ω)	1.2, 2.4	2.8
L_s	Filter reactance (Ω)	1.92, 3.84	27.97
R_g	TL losses (Ω)	0.4	0.79
L_g	TL reactance (Ω)	1.85	6.57
R_l	Load resistance (Ω)	8.7	95.22
L_f	Load inductive reactance (Ω)	10.21	108.19
C_f	Load capacitive reactance (Ω)	-24.11	-176.83
f_s	Switching frequency (kHz)	6.6	6.6

cated that the controller can operate in more extreme scenarios with parameters representative of a 13.8 kV microgrid.

The ability of the controller to limit the converter output current during a worst-case fault condition has been demonstrated. This finding is significant, as overcurrent limiting is not inherent to a voltage-based control strategy. Peak fault currents are further limited through the use of dynamic limiting.

The addition of the islanding detection feature shows that this control scheme can be modified to accurately determine the islanded status of the microgrid, with the disadvantage of slightly increasing the time for which the load is exposed to a hard violation if islanding due to a fault.

The purpose of the work presented in this paper was to show that the voltage-control strategy under study is viable for use in multiple-source microgrid applications and to characterize and demonstrate its overcurrent protection and islanding detection features. This has been achieved through simulation and experimental verification by using a prototype system.

APPENDIX SYSTEM PARAMETERS

Single parameters imply use for all sources present in the system. For parameters variations between sources, values have been separated by commas.

REFERENCES

- [1] T. Ackermann, "Distributed generation: A definition," *Elect. Power Syst. Res.*, vol. 57, no. 3, pp. 195–204, 2001.
- [2] R. Lasseter, A. Akhil, C. Marnay, J. Stephens, J. Dagle, R. Guttromson, A. S. Meliopoulos, R. Yinger, and J. Eto, "The CERTS microgrid concept," Tech. Rep. LBNL-50829, Apr. CERTS, 2002.
- [3] C. Rehtanz, *Autonomous Systems and Intelligent Agents in Power System Control and Operation*. Berlin, Germany: Springer, 2003.
- [4] P. Piagi and R. H. Lasseter, "Autonomous control of microgrids," presented at the IEEE Power Eng. Soc. Gen. Meeting, Montreal, QC, Canada, Jun. 2006.

- [5] J. A. P. Lopes, C. L. Moreira, and A. G. Madureira, "Defining control strategies for microgrids islanded operation," *IEEE Trans. Power Syst.*, vol. 21, no. 2, pp. 916–924, May 2006.
- [6] F. Gao and M. R. Iravani, "A control strategy for a distributed generation unit in grid-connected and autonomous modes of operation," *IEEE Trans. Power Del.*, vol. 23, no. 2, pp. 850–859, Apr. 2008.
- [7] H. Zeineldin, E. F. El-Saadany, and M. M. A. Salama, "Intentional islanding of distributed generation," in *Proc. IEEE Power Eng. Soc. Gen. Meeting*, 2005, vol. 2, pp. 1496–1502.
- [8] M. Prodanovic and C. Green, "Control of inverter-based micro-grids," *Elect. Power Syst. Res.*, vol. 77, no. 9, pp. 1204–1213, Jul. 2007.
- [9] M. Prodanovic, "A survey of control methods for three-phase inverters in parallel connection," in *Proc. 8th Int. Conf. Power Electron. Variable Speed Drives*, 2000, vol. 2000, pp. 472–477.
- [10] K. Siri, C. Q. Lee, and T.-E. Wu, "Current distribution control for parallel connected converters. I," *IEEE Trans. Aerosp. Electron. Syst.*, vol. 28, no. 3, pp. 829–840, Jul. 1992.
- [11] W. Bower and M. Ropp, "Evaluation of islanding detection methods for utility-interactive inverters in photovoltaic systems," Sandia Nat. Labs., Livermore, CA, Tech. Rep. SAND2002-3591, 2002.
- [12] R. H. Lasseter, "Microgrids," in *Proc. IEEE Power Eng. Soc. Winter Meeting Conf.*, 2002, vol. 1, pp. 305–308.
- [13] M. N. Marwali, J. W. Jung, and A. Keyhani, "Control of distributed generation systems—Part II: Load sharing control," *IEEE Trans. Power Electron.*, vol. 19, no. 6, pp. 1551–1561, Nov. 2004.
- [14] Y. Li, D. M. Vilathgamuwa, and P. C. Loh, "Design, analysis, and real-time testing of a controller for multibus microgrid system," *IEEE Trans. Power Electron.*, vol. 19, no. 5, pp. 1195–1204, Sep. 2004.
- [15] F. Katiraei, M. R. Iravani, and P. W. Lehn, "Micro-grid autonomous operation during and subsequent to islanding process," *IEEE Trans. Power Del.*, vol. 20, no. 1, pp. 248–257, Jan. 2005.
- [16] C. A. Plet, M. Graovac, T. C. Green, and R. Iravani, "Fault response of grid-connected inverter dominated networks," in *Proc. IEEE Power Eng. Soc. Gen. Meeting*, Jul. 2010, pp. 1–8.
- [17] *Inverters, Converters, Controllers and Interconnection System Equipment for use With Distributed Energy Resources*, UL 1741, Underwriters Labs, 2002.
- [18] F. Martin, "Development of a PC-based control platform for power electronic using real-time Linux with application to a unified power flow controller," M.A.Sc. degree, Dept. Elect. Comput. Eng., Univ. Toronto, Toronto, ON, Canada, 2002.
- [19] S. Doebla, "Development of a real time control and monitoring environment," M.A.Sc. dissertation, Dept. Elect. Comput. Eng., Univ. Erlangen-Nürnberg, Erlangen-Nürnberg, Germany, 2002.
- [20] RT-Linux GPL. [Online]. Available: <http://www.rtlinuxfree.com/>
- [21] J. Bloemink, "Validation of a novel approach to voltage sourced converter control for MicroGrid operation," M.Sc. dissertation, Dept. Elect. Comput. Eng., Univ. Toronto, Toronto, ON, Canada, Oct. 2007.



Jeffrey M. Bloemink (S'05) received the B.A.Sc. and M.A.Sc. degrees in electrical engineering from the University of Toronto, Toronto, ON, Canada, in 2005 and 2007, respectively, and is currently pursuing the Ph.D. degree in electrical engineering at Imperial College London, London, U.K.

His research interests include the integration of power electronics for compensation of distribution systems as well as distributed generation coordination and control.



M. Reza Iravani (M'85–SM'00–F'03) received the B.Sc. degree in electrical engineering from Tehran Polytechnic University, Tehran, Iran, in 1976, and the M.Sc. and Ph.D. degrees in electrical engineering from the University of Manitoba, Winnipeg, MB, Canada, in 1981 and 1985, respectively.

Currently, he is a Professor at the University of Toronto, Toronto, ON, Canada. His research interests include power electronics and power system dynamics and control.